CHAPTER 4

Results and discussion

This chapter describes the results and discussion of the experiment which was done according to the procedure in chapter 3. The obtained products were analyzed by XRD, SAED, HRTEM, SEM, Raman, FTIR and PL characterization. Gas sensing performance was also studied by exposing the materials, p-type (CuO), to reducing gas environment. The experimental results were compared with other previous works and discussed in details.

4.1 MoO_3

4.1.1 XRD, SAED and HRTEM

XRD patterns of the products processed for 40, 50 and 60 min are shown in Figure 4.1. Their peaks were specified as orthorhombic MoO_3 of JCPDS database no.05-0508 [83], with no impurity detection. The (020) peaks at 2θ of 12.8º were clearly detected, and indicated the presence of orthorhombic phase instead of monoclinic [84]. It should be noted that their intensities were slightly increased with the increase of processing time. The XRD peaks for 60 min processing time were the strongest, reflecting the product with the best degree of crystallinity. During processing, $(NH_4)_6Mo_7O_{24}\cdot 4H_2O$ decomposed as follows:

$$(NH_4)_6Mo_7O_{24}\cdot 4H_2O(s) \rightarrow 7MoO_3(s) + 6NH_3(g) + 7H_2O(g) \quad (4.1)$$

$MoO_3(s)$ was left as the final solid products. Two gases (NH_3 and H_2O) diffused out of the system, and evacuated out of the horizontal quart tube. It should be noted that some reactant could remain, and was mixed with

the final product if the processing time was less than 40 min. Longer processing times resulted in greater purification of the final product. Calculated lattice parameters (Å) using the plane spacing equation for orthorhombic phase[85] were a = 3.96, b = 13.86 and c = 3.70, in accordance with those of the JCPDS database [83]. Figure 4.2 (a) shows the SAED pattern of a single crystal processed for 60 min. It was indexed [86] to correspond with the (002), (202) and (200) crystallographic planes, which were specified as orthorhombic α-MoO_3 [83,87]. In the present analysis, an electron beam was sent to the crystal along the [010] direction. The (021) crystallographic plane with 0.33 nm spacing was detected by HRTEM (Figure 4.2 b), implying that the product was crystalline in nature. These last two analyses were in accordance with that of the above XRD.

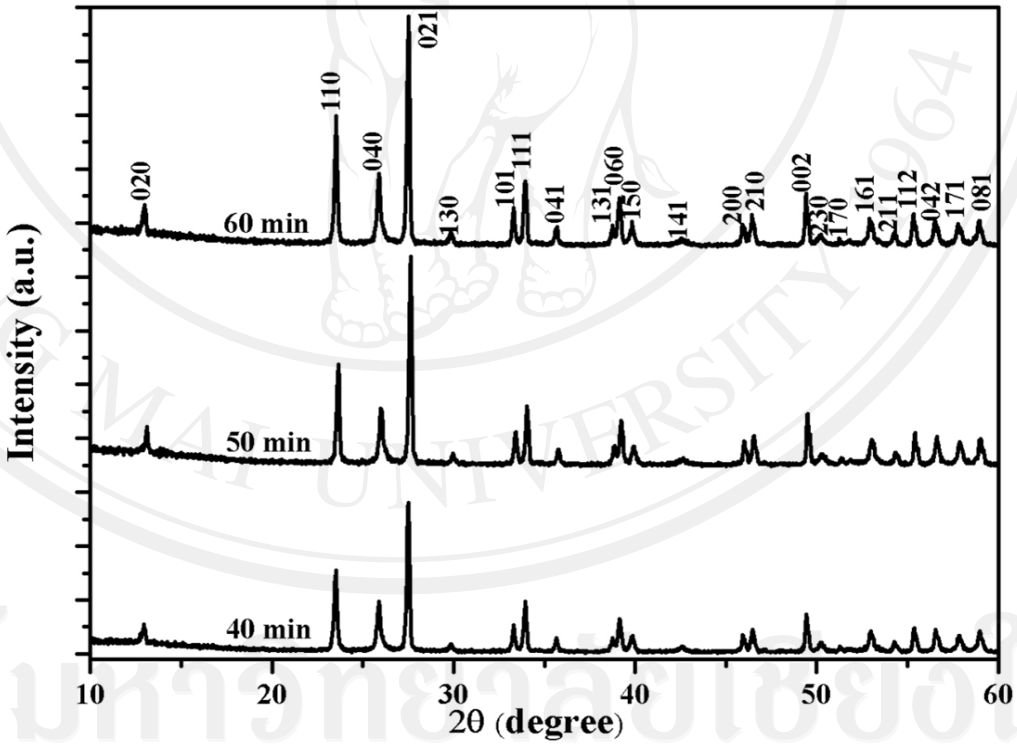

Figure 4.1 Diffractrogram of α-MoO_3 processed for 40, 50, and 60 min.

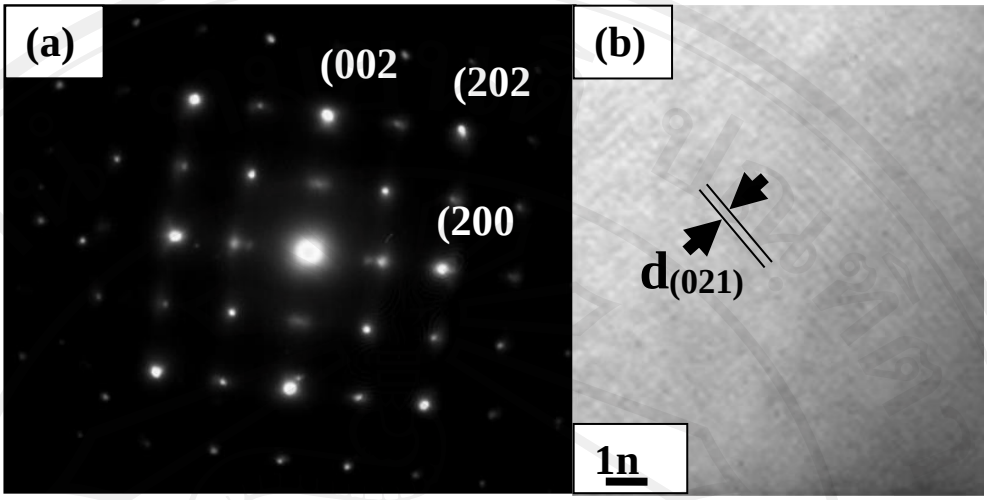

Figure 4.2 (a) SAED pattern and (b) HRTEM image of α-MoO_3 processed for 60 min.

4.1.2 SEM

SEM images of MoO_3 crystals processed for 40, 50 and 60 min are shown in Figure 4.3-4.6. Clusters of spheres ranging from 100 nm to a few hundred nm, as well as a small fraction of plates, were produced by 40 min processing. When the processing time was 50 min, more plates about 100 nm thick and a few μm long were produced, growing perpendicular to the cluster surface. Sixty min processing resulted in a further increase in the number of plates produced, as well as their sizes of 100–200 nm thick and a few μm long. During processing, some plates could be broken due to the internal stress developed in structure.

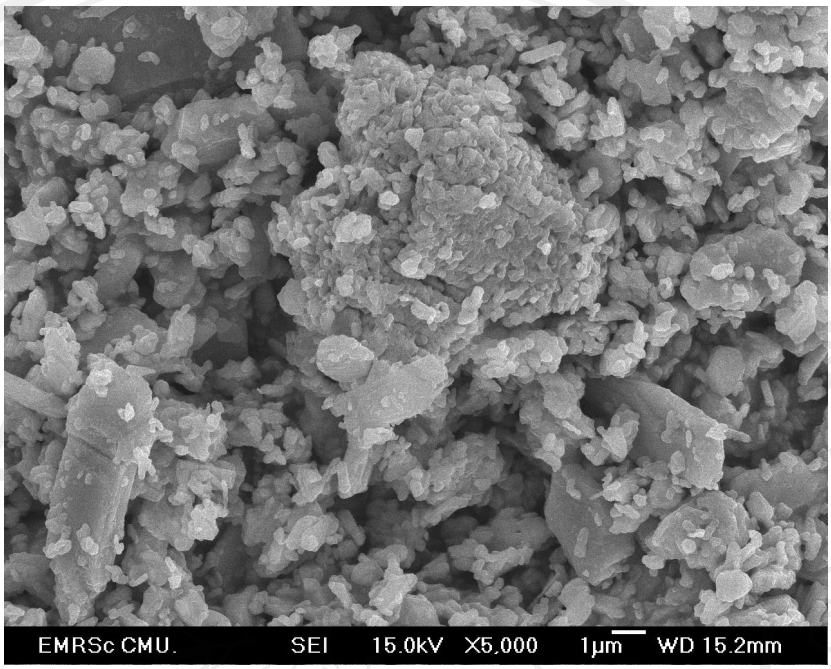

Figure 4.3 SEM image of MoO_3 crystal processed for 40 min.

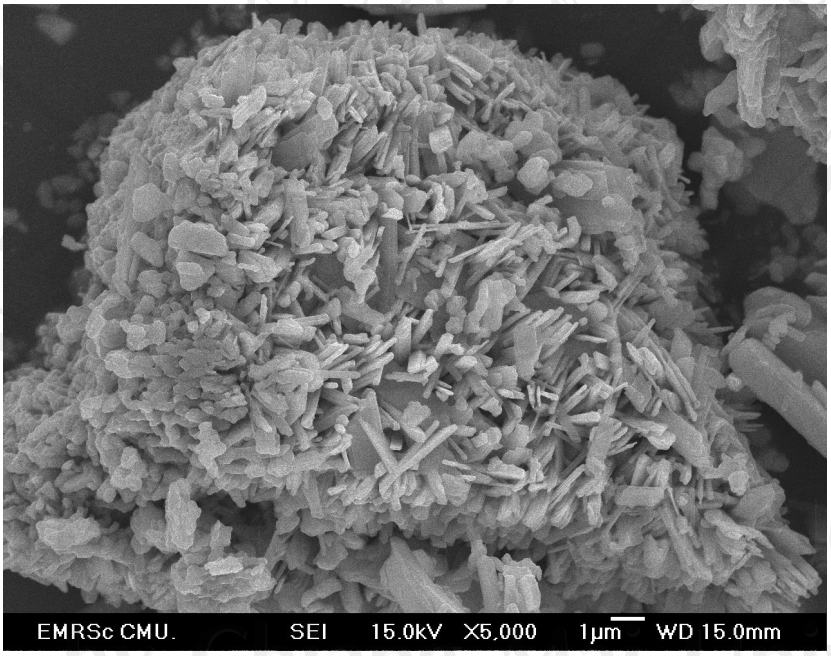

Figure 4.4 SEM image of MoO_3 crystal processed for 50 min.

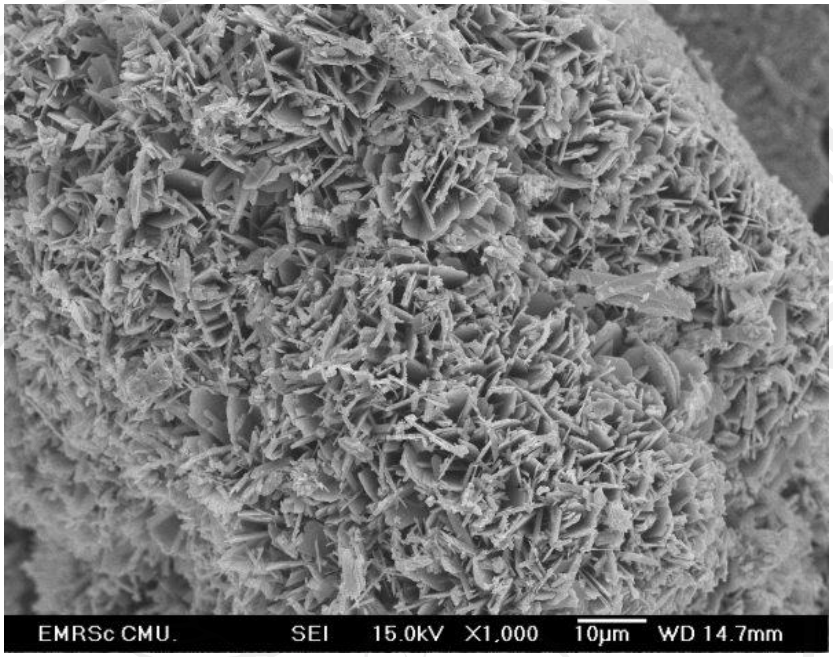

Figure 4.5 SEM image of MoO_3 crystal processed for 60 min (x 1,000).

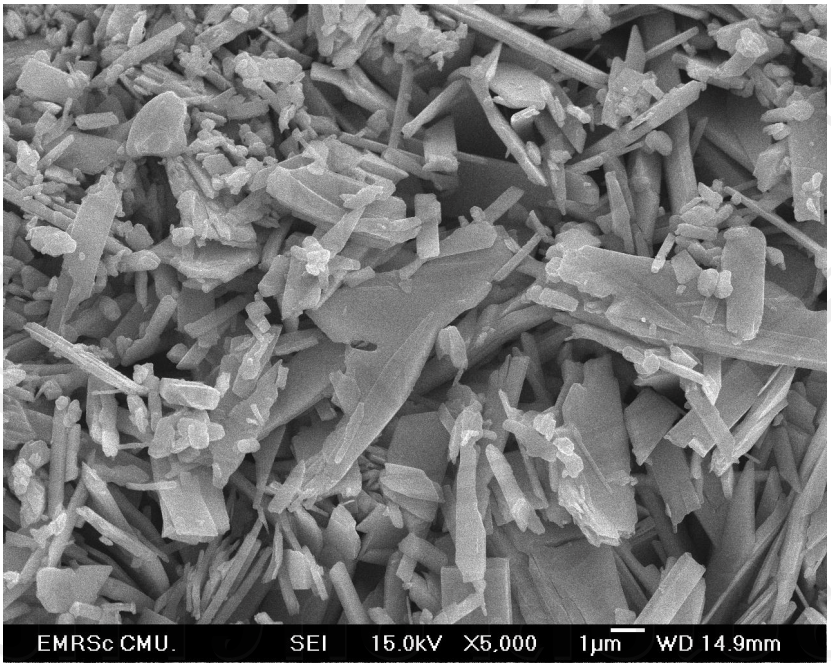

Figure 4.6 SEM image of MoO_3 crystal processed for 60 min (x 5,000).

4.1.3 Raman and FTIR analyses

Raman spectra (Figure 4.7 a) of MoO_3 crystals processed for 40, 50 and 60 min were studied in the range of 150–1050 cm^{-1}. During the analysis, a low-intensity laser was used to avoid crystallization. The product of 60 min processing was highly ordered crystalline structure, and its Raman peak was the highest. The height was reduced when the processing time was shortened. In the present research, 12 typical Raman peaks were detected. The peaks at 990 cm^{-1} were specified as the Mo═O asymmetric stretching modes of terminal (unshared) oxygen [87]. The strongest peaks were at 813 cm^{-1}, and were specified as the doubly connected bridge-oxygen Mo_2─O stretching modes [88] of doubly coordinated oxygen, caused by corner-shared oxygen atoms in common to two MoO_6 octahedrons [87]. The peaks at 666 cm^{-1} were the Mo_3─O stretching modes of triply coordinated bridge-oxygen, caused by edge-shared oxygen atoms in common to three octahedrons [87,88]. Their remains were the O─Mo─O asymmetric stretching/bending modes at 470 cm^{-1}, O─Mo─O scissoring modes at 378 and 364 cm^{-1}, O─Mo─O bending modes at 337 cm^{-1}, O═Mo═O wagging modes at 287 cm^{-1}, O═Mo═O twisting modes at 244 cm^{-1}, R_c modes at 217 cm^{-1}, O═Mo═O twisting modes at 197 cm^{-1}, and T_b modes at 158 cm^{-1} [87]. Sometimes the Raman peaks were positively/negatively shifted, due to the increase or decrease in the vibration constant of the products [88]. In the present research, the vibrations were the same values, although the processing time and degree of crystallinity were different.

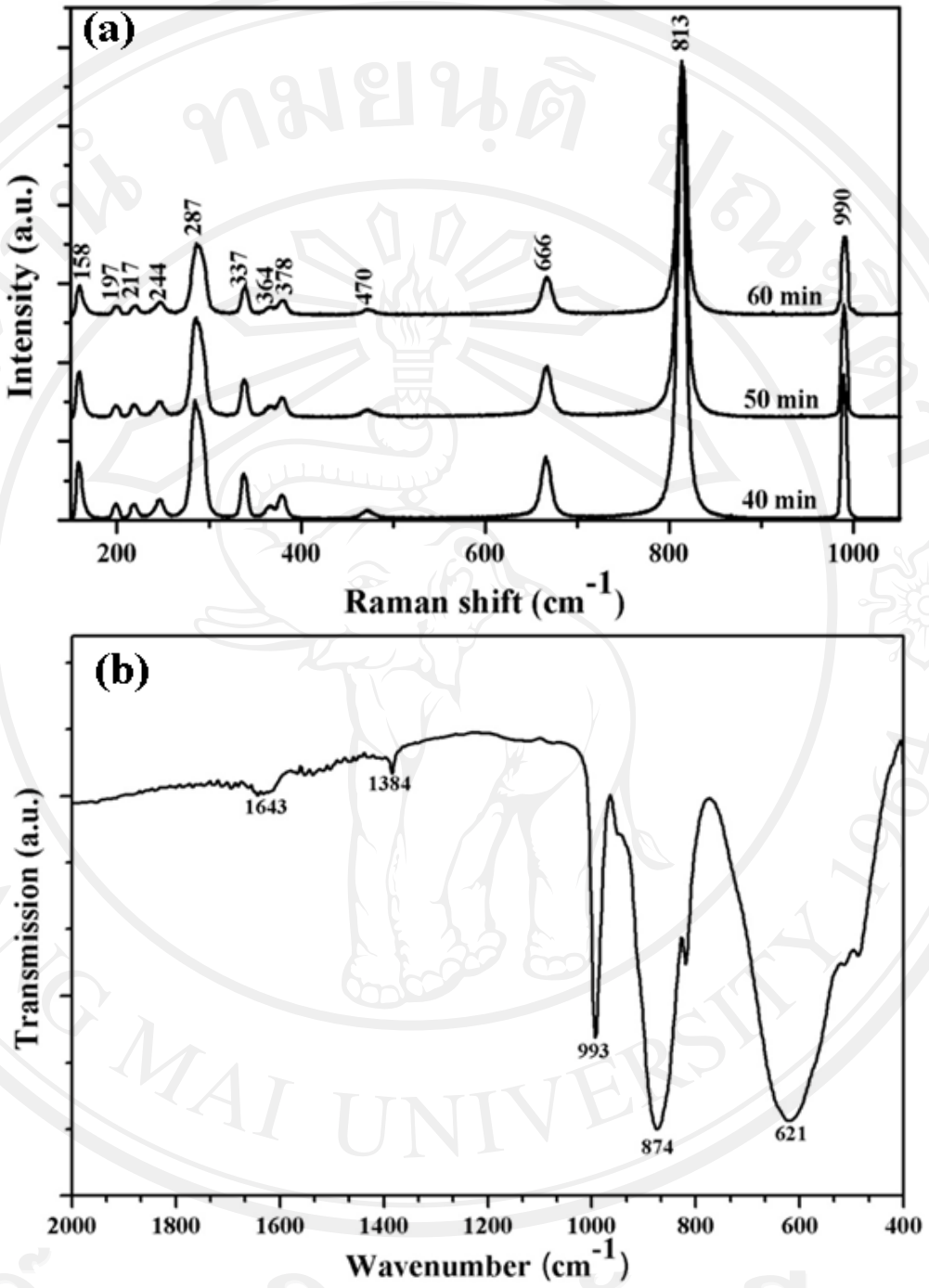

Figure 4.7 (a) Raman analysis of α-MoO_3 processed for 40, 50 and 60 min.
(b) FTIR spectrum of α-MoO_3 processed for 60 min.

Figure 4.7 b shows the FTIR spectrum of α-MoO_3 over the 400–2,000 cm^{-1} range. Three strong vibrations were detected at 621, 874 and 993 cm^{-1}, associated respectively with the stretching mode of oxygen linked with three metal atoms, the stretching mode of oxygen in the Mo─O─Mo units, and the Mo═O stretching mode – the specification of a layered orthorhombic α-MoO_3 phase. Two weak vibrations were also detected at 1,384 and 1,643 cm^{-1}, associated with the vibration mode of the Mo─OH bond and the bending mode of adsorbed water, respectively [89,90].

4.1.4 PL emission

PL emission of orthorhombic α-MoO_3 processed for 40, 50 and 60 min was studied using 380 nm excitation wavelength at room temperature. The PL spectra (Figure 4.8) presented broad peaks over the 400–600 nm range with a strong indigo emission centered at 430–440 nm in accordance with the report of Song [91]. These emissions were caused by the band-to-band transition. In the present research, very weak shoulders, caused by the electron-hole recombination between the conduction band and the sub-level of adsorbed oxygen acceptors, were also detected; these were able to be reduced by calcination at high temperatures [91] The luminescence intensity increased with the increase of processing time, in accordance with the improvement of the degree of crystallinity characterized by the above XRD analysis.

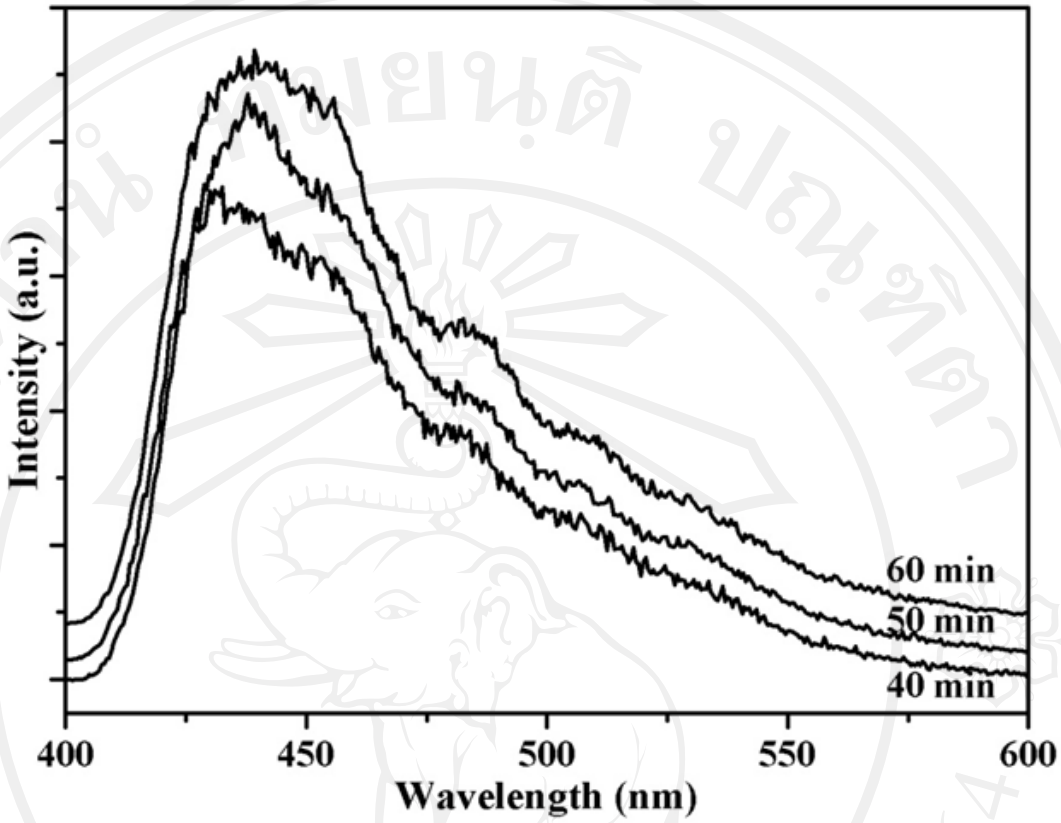

Figure 4.8 PL emission of α-MoO_3 processed for 40, 50, and 60 min.

4.2 CuO

4.2.1 XRD

The XRD patterns of the 50A and 3.6 V as-synthesized powder at different length of processing time are shown in Figure 4.9. According to the JCPDS database, all diffraction peaks can be indexed as follows. For 1 min processing time, the solid mixture of cubic Cu (JCPDS No.004-0836) and cubic Cu_2O (JCPDS No.078-2076) were detected. Monoclinic CuO (JCPDS No. 048-1548) was revealed as a component of mixture at 3 min heating time. Cu peaks became a small fraction at 6 min and were no longer detected when the processing time was reach 9 min. At 12 min processing time, Cu_2O still contains as an impurity of CuO main phase. For the 15 min processing time, crystalline CuO was successfully synthesized without

any impurity detection. During processing, oxygen gradually diffused into Cu matrix and formed Cu_2O as a primary metal oxide. Then the Cu_2O crystal transformed into CuO, described by the following equation: $2Cu_2O + O_2 \rightarrow 4CuO$ [92]. The prolonged time of batch processing was able to enrich oxygen to further oxidize Cu^{1+} to Cu^{2+}. The conversion of Cu_2O to CuO at the temperature above 400 ^oC was reported [93].

The lattice constants of CuO pure phase were calculated using the least square refinement from the UNITCELL-97 program [94]. The calculated lattice parameters (a = 4.6922 Å, b = 3.4253 Å and c = 5.1340 Å with $\beta = 99.4575^o$) are in accordance with those of the JCPDS No. 048-1548 with lattice constants of a = 4.6883 Å, b = 3.4229 Å, c = 5.1319 Å, and $\beta = 99.5060^o$.

The average size of crystallite (G_{hkl}) was estimated by the classical Scherrer's formula

$$G_{hkl} = \frac{0.9\lambda}{D\cos\theta} \qquad (4.2)$$

where λ is the wavelength of the incident X-ray (Cu-K_α radiation source with 0.15418 nm), D is the full width at half maximum (FWHM) and θ is the Bragg's angle. The (111) strongest peak was used for calculation. The crystallite size for 15 min heating time is143 nm.

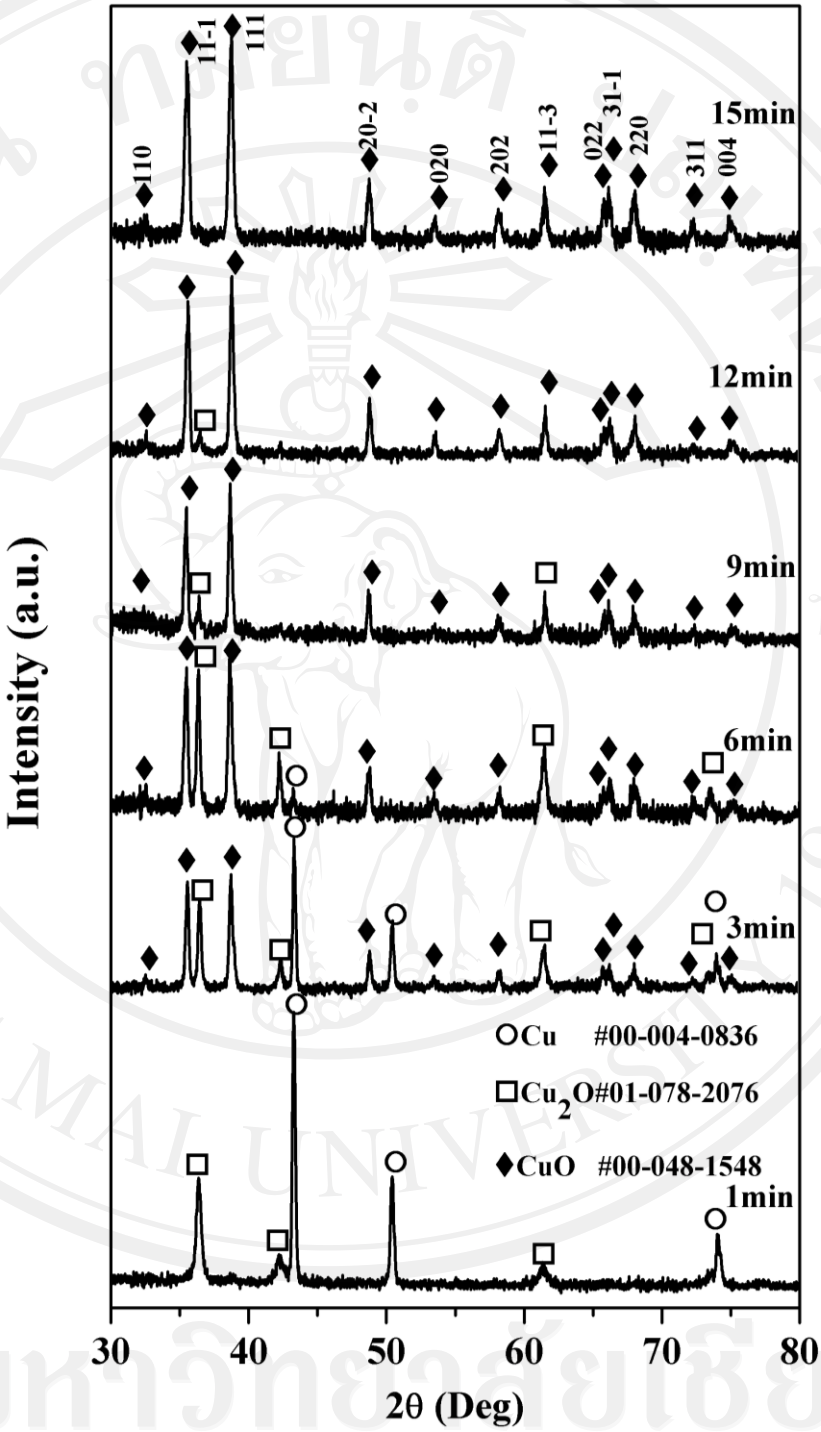

Figure 4.9 XRD patterns of the samples synthesized for 1, 3, 6, 9, 12 and 15 min processing time.

4.2.2 TEM and SEM

The morphology of the samples was examined by SEM and TEM. In this research, the as-synthesized samples were studied without any further processing. TEM image of the 15 min processing time is shown in Figure 4.10a. The particle has an irregular shape with 433 nm in length and 305 nm in width. Crystalline structure of 15 min processing time was also simulated by VESTA version 3.0 program as shown in Figure 4.10b.

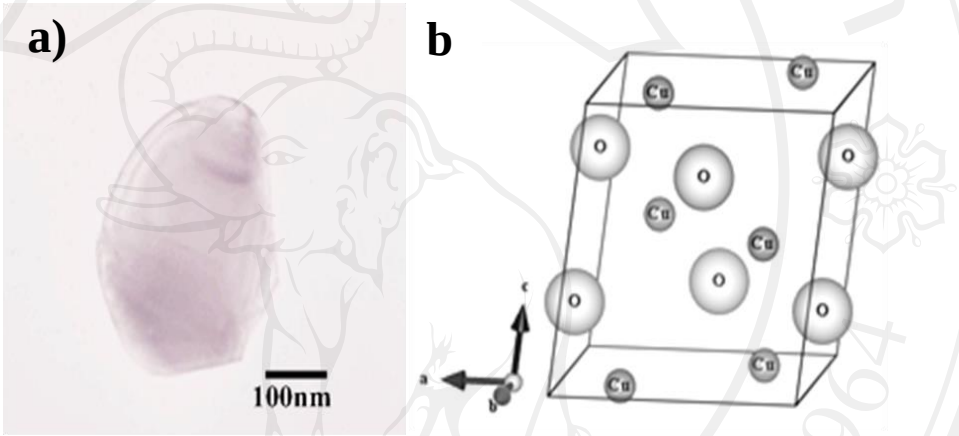

Figure 4.10 TEM image of the 15 min as-synthesized CuO sample and its simulated crystalline structure.

The morphology of the samples was examined by SEM. Figure 4.11 - 4.16 shows typical SEM images of the as-synthesized samples composing of agglomerated particles with irregular shape. For 1 min long, Cu particles melt to form as necking of the surrounding particles. Initially, particles have an average diameter of 2.75μm. Oxygen slightly diffused into Cu matrix and changed the surface of Cu by forming metal oxide phase. When the processing times were complete at 3 min and 6 min and the system was cooled down, oxides at the surface separated from metal precursors due to the difference of their thermal expansion coefficient. Upon processing at the interval of 9 min, 12 min and 15min, the particles were reduced in size due to metal oxide formation. In addition, metal oxide particles have dense

agglomeration indicating the sintering process. The particles were approximately 450 nm in diameter within 15 min processing.

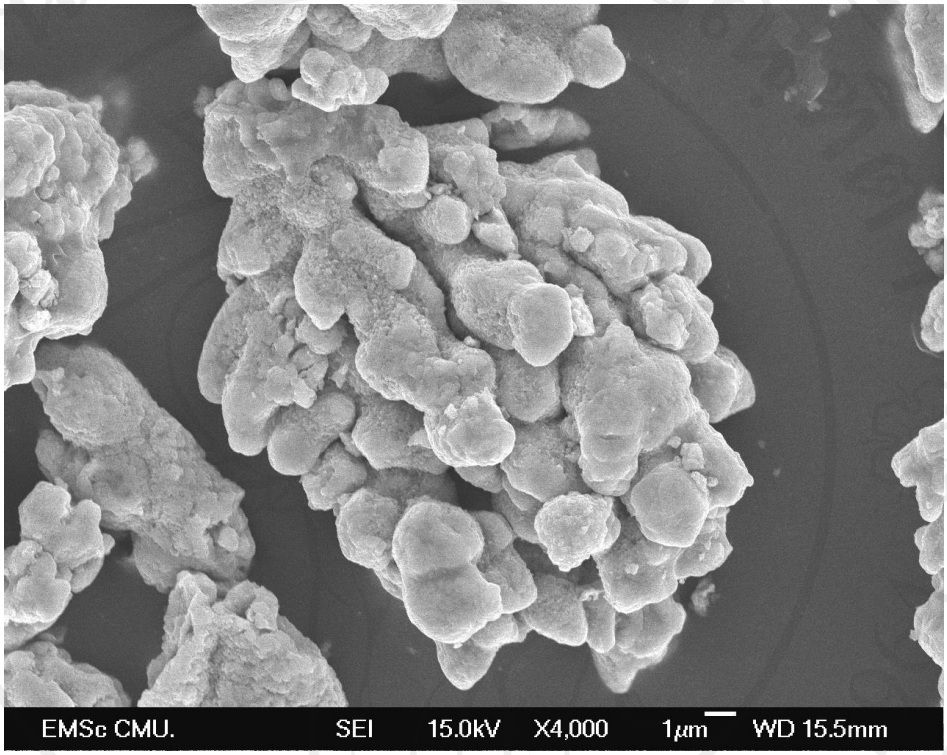

Figure 4.11 SEM image of the sample synthesized for 1 min.

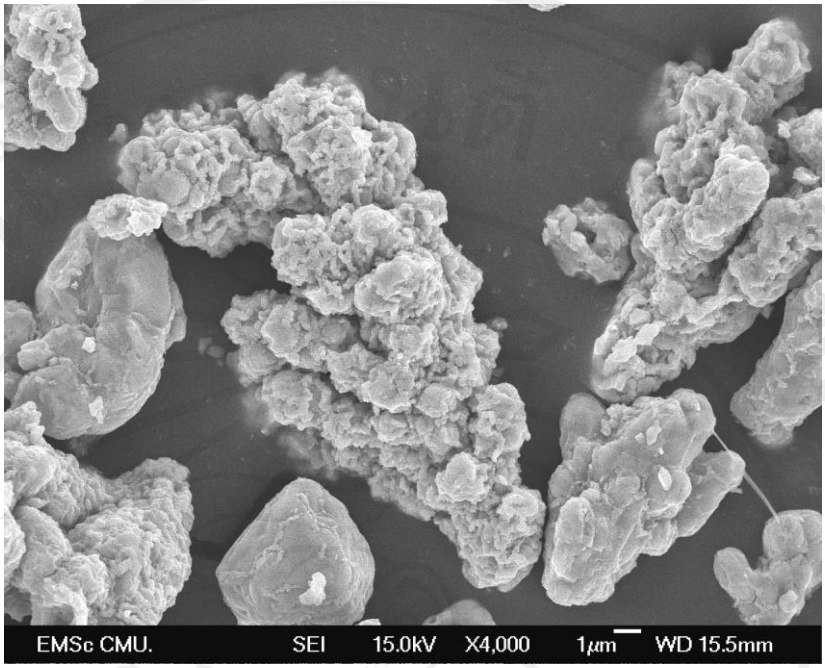

Figure 4.12 SEM image of the sample synthesized for 3 min.

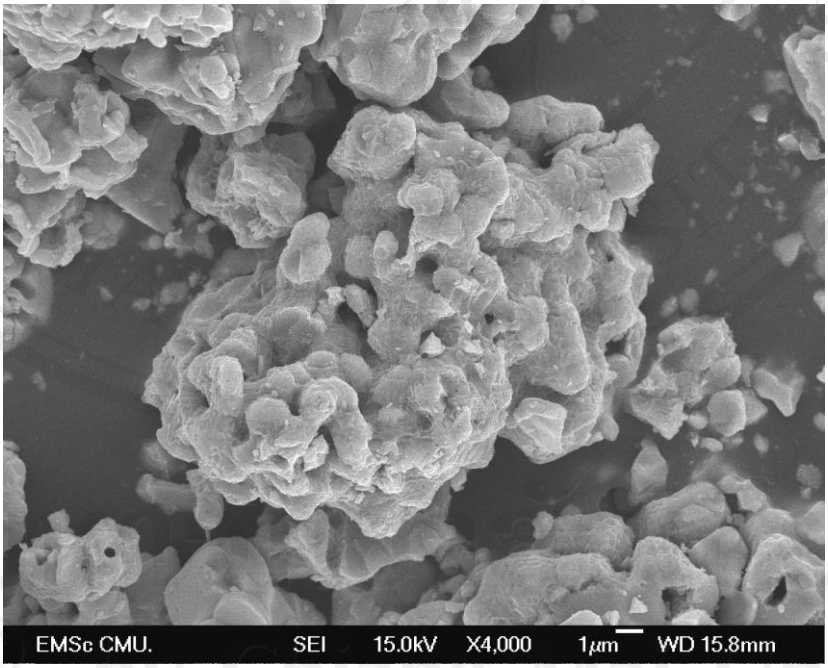

Figure 4.13 SEM image of the sample synthesized for 6 min.

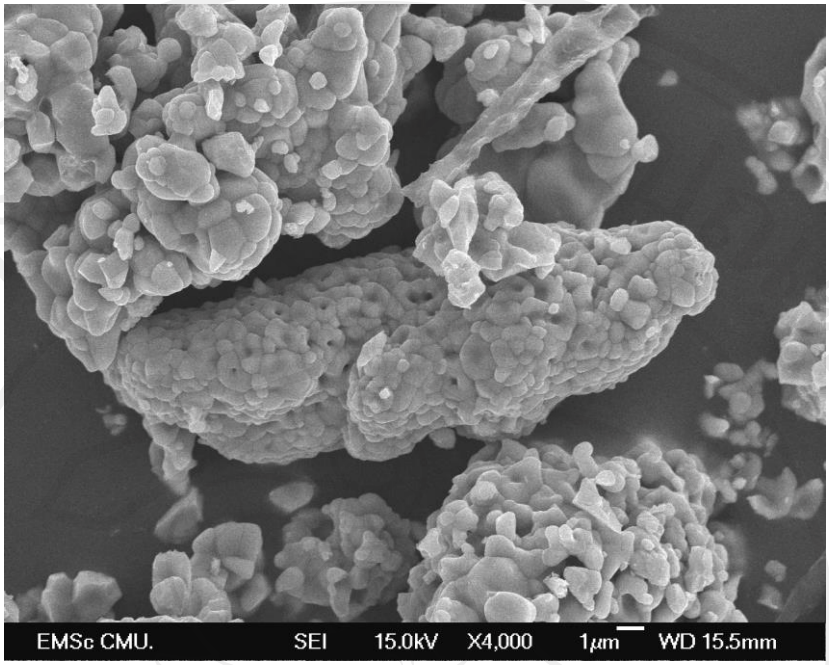

Figure 4.14 SEM image of the sample synthesized for 9 min.

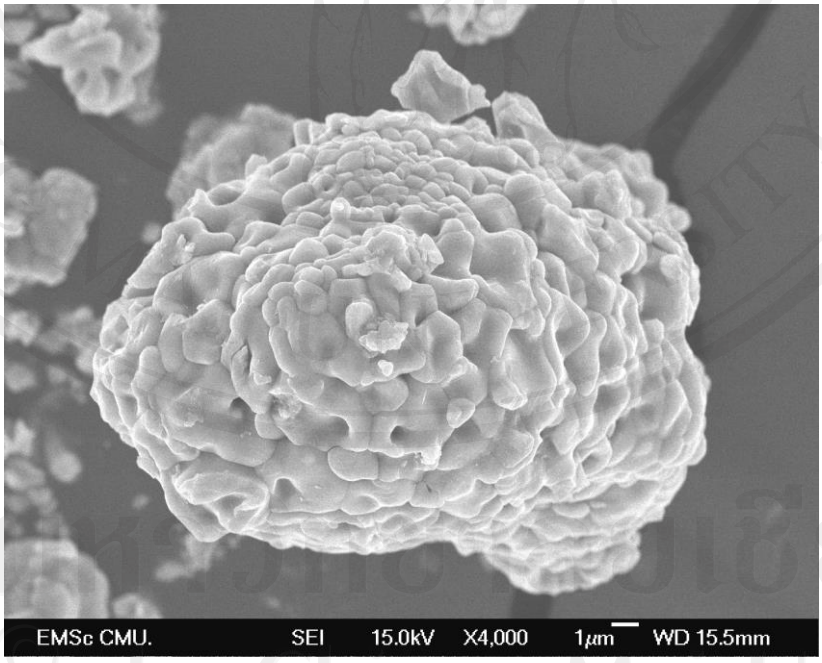

Figure 4.15 SEM image of the sample synthesized for 12 min.

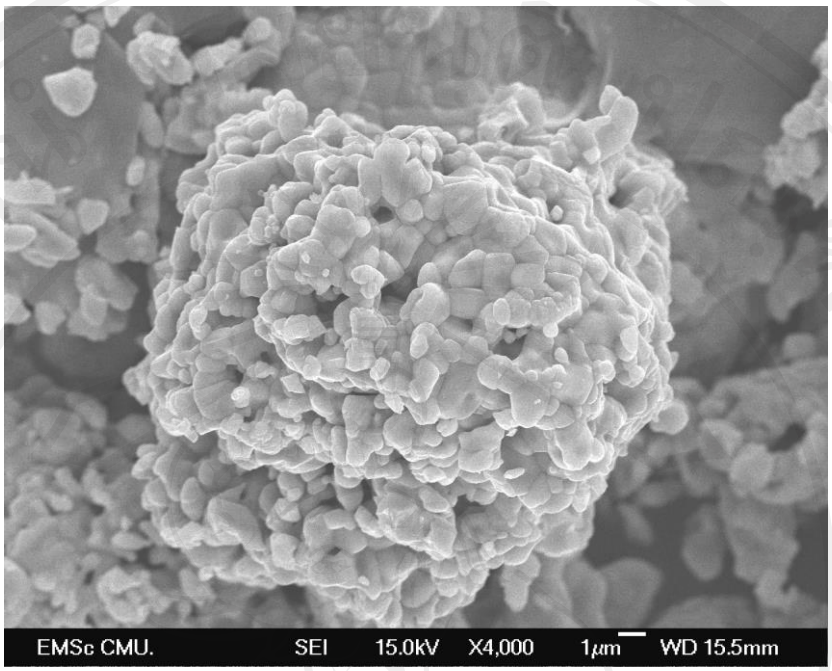

Figure 4.16 SEM image of the sample synthesized for 15 min.

4.2.3 FTIR

FTIR spectra of samples are shown in Figure 4.17. The as-synthesized samples exhibit absorption bands at approximately 3250–3600 cm^{-1} which can be specified as O−H stretching contributed by water content. The absorption band at 1383 cm^{-1} was the result of Cu^{2+}–O^{2-} stretching mode peak, which was very close to the report of Li [95] at 1384 cm^{-1}. FTIR spectra detected at 529 cm^{-1} and 585cm^{-1} can be indexed to the vibrational mode of CuO formation with good corresponding to the result of Vellora [96] at 525 and 580 cm^{-1}. For 1 min processing, a peak appear at 621 cm^{-1} corresponding to Cu (I)–O vibrational mode [97], in accordance with the XRD analysis, showing Cu_2O phase in the sample at the same length of operating time.

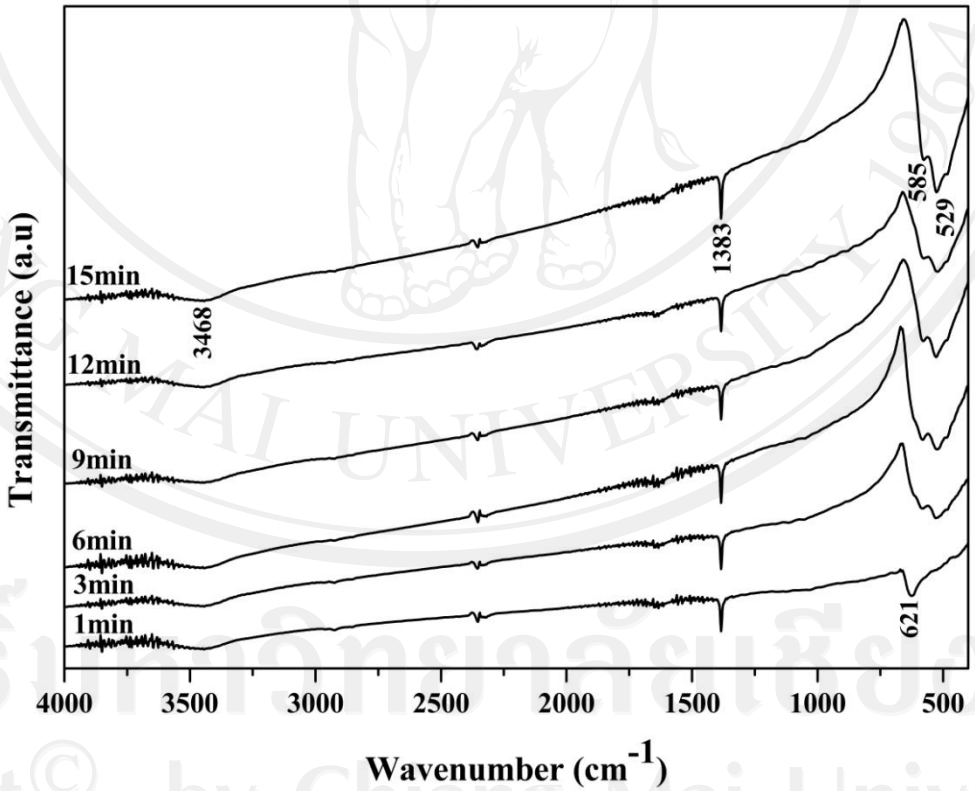

Figure 4.17 FTIR spectra of the samples synthesized for 1, 3, 6, 9, 12 and 15 min processing time.

4.2.4 PL and UV-Vis

Photoluminescence (PL) spectrum of the 15 min processed sample was determined at room temperature as shown in Figure 4.18. The excitation energy from a Xe arc-lamp at 325 nm wavelength was used. The main emission peak was observed around 402 nm in the violet region. The result is in good agreement with the report of Mukherjee [98], Chang [99] and Maji [100] who reported the emission wavelengths at 395 nm, 403 nm and 406 nm, respectively. The reason of the emission is still unclear because a few reports are available on the PL emission spectra of CuO. The previous study of CuO had claimed that the emission peak was caused by the blue shifted emission comparing to the bulk counterpart [98]. The broad shoulder peak shows in the green spectral region corresponding to the study of Chang [99]. According to the above XRD analysis, the samples processed for 1, 3, 6, 9 and 12 min were mixtures of different phases. Thus they are not interesting to be determined the PL emission.

The theory of inter-band absorption shows that at the fundamental edge the absorption coefficient should vary according to the equation [101]

$$\alpha h\nu = B(h\nu - E_o)^n \qquad (4.3)$$

where $h\nu$ is the photon energy in eV, α is the absorption coefficient in cm^{-1}, B is a constant related to the material and the matrix element of the transition, E_o is the optical energy gap, and n is a pure number which characterizes the transition process: n = 1/2 for direct allowed, n = 2 for indirect allowed, n = 3/2 for direct forbidden, and n = 3 for indirect forbidden transitions. The absorption coefficient was calculated using the relation $\alpha d = \ln(1/T)$ where the transmittance T was calculated from the measured absorbance using Beer–Lambert law $A = -\log_{10}(T)$. Here d stands for the path length of the wave in cm and was set equal to the cuvette width of 1 cm.

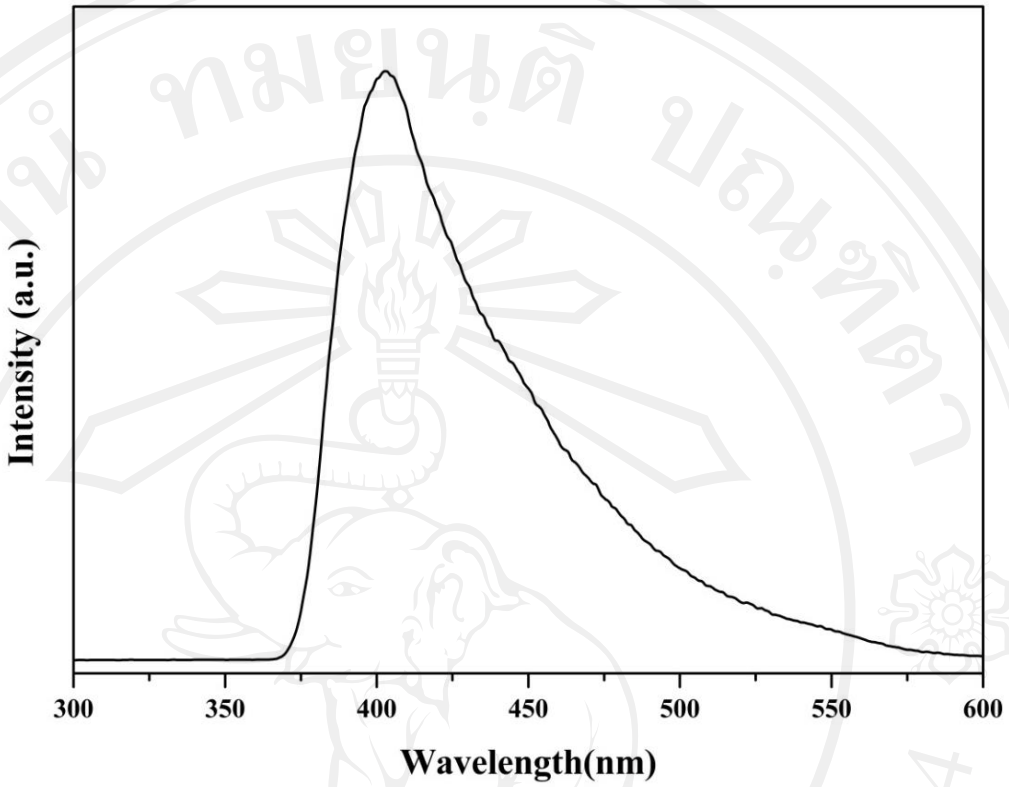

Figure 4.18 PL peak of CuO processed for 15 min.

According to Wood and Tauc equation for photonic absorbance, the energy E_o can be estimated from the slope and intercept of the linear plot of $(\alpha h\nu)^2$ versus $h\nu$. This dependence is typical of direct allowed transition. From the data of Figure 4.19, the energy gap (E_o) is 3.95 eV. This value is close to the report of Kidowaki [102] showing at 3.70 eV and Rehman [103] at 3.72 eV for 20 nm particles. Furthermore, Rehman [103] gave the reason to determine energy gap in direct transition because absorption spectroscopy detecting from indirect transition of CuO by using the UV–VIS–NIR is weak.

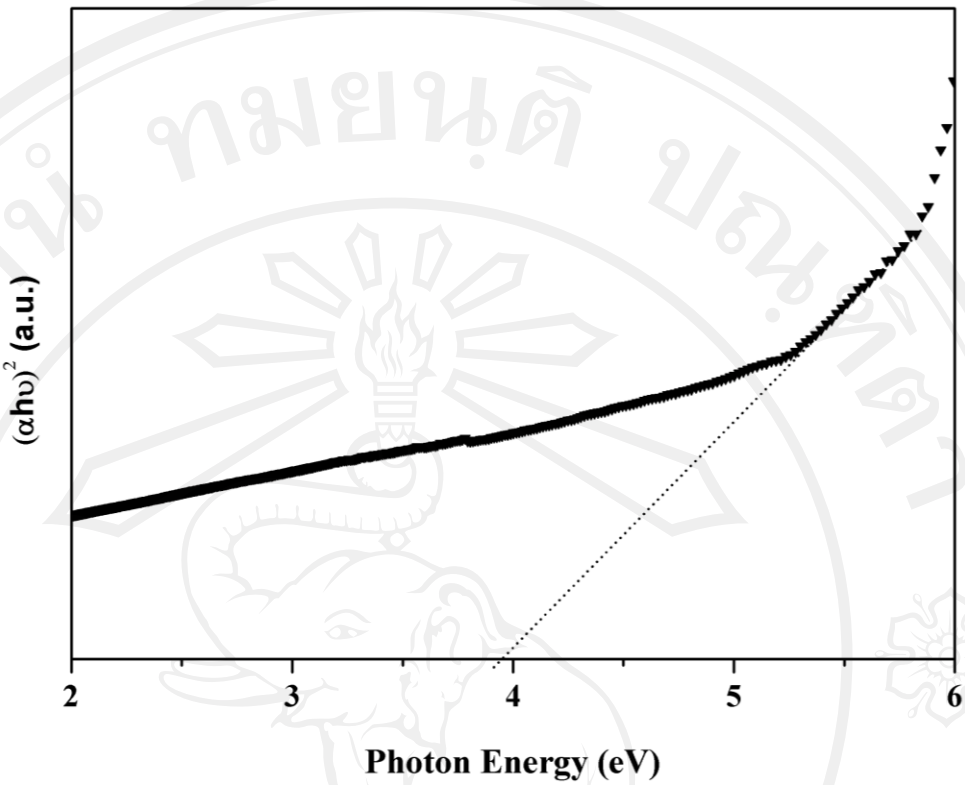

Figure 4.19 Direct band gap estimation of 15 min synthesized CuO.

4.2.5 XPS

The surface characterization of the 15 min processed sample was determined by XPS as shown in Figure 4.20. The peaks located at 933.8 eV and 953.8 eV are attributed to the Cu $2p_{3/2}$ and Cu $2p_{1/2}$, respectively[104]. The Cu $2p_{3/2}$ peak can be assigned to two Cu–O formation processes (CuO at 933.7 eV and Cu_2O at 932.5 eV) [105]. It is an indicator of the Cu(II) oxidation state. The peaks at 941.7 eV, 944.0 eV and 962.3 eVare assigned to the shaking up lines. The spectrum of O 1s has the range between 527–535 eV. The peak at 530.1 eV is related to O^{2-} in CuO and at 531.3 is attributed to oxygen adsorb on the surface of CuO[106]. The intensity of peak at 530.1 eV is stronger than that at 531.3 eV that relied on the adsorbed oxygen rather than O ions in Cu^{2+}–O^{2-} formation. No impurities were detected by the XPS. Thus it is reasonable to confirm that the as-synthesized sample was CuO.

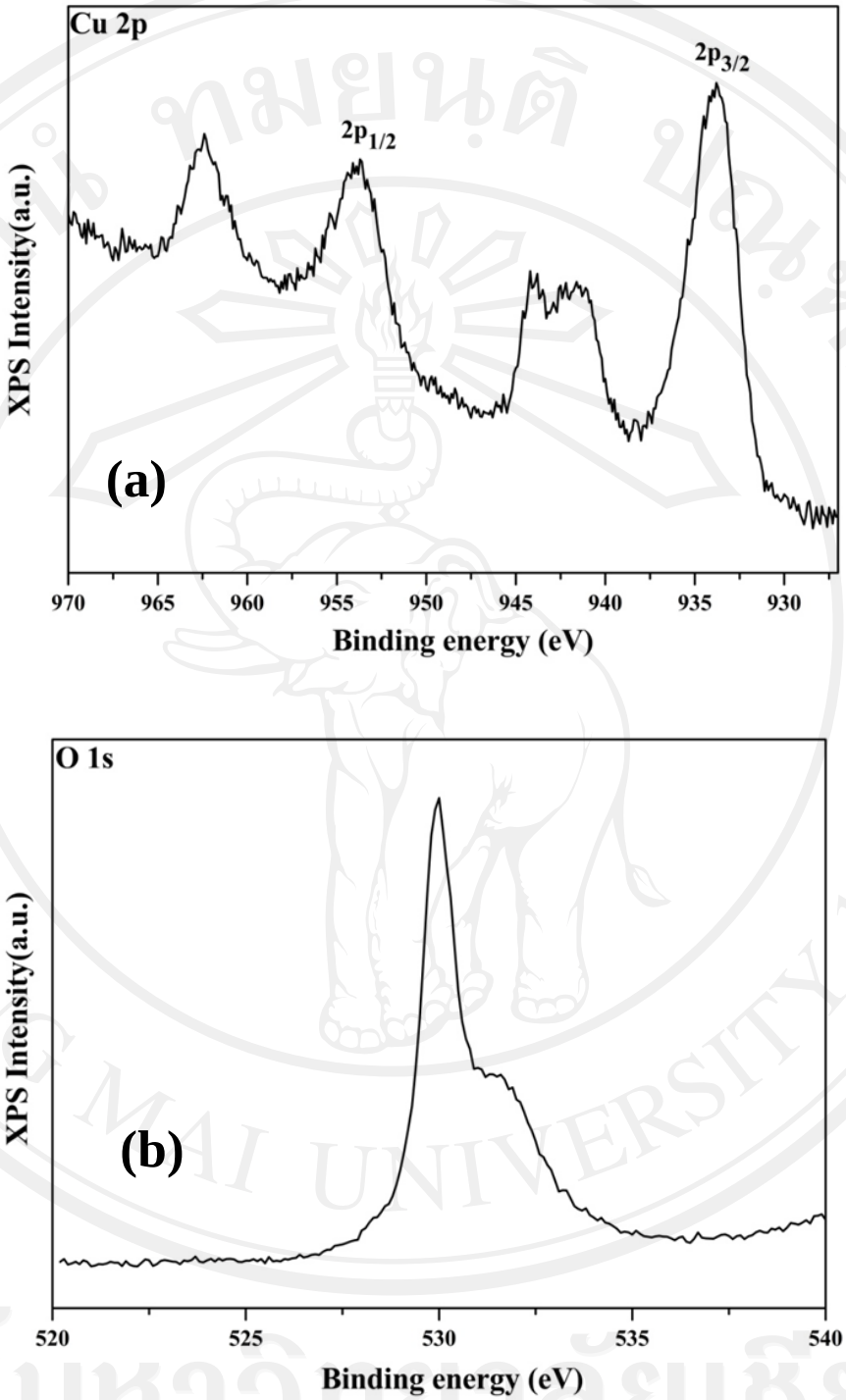

Figure 4.20 XPS spectra of the 15 min as-synthesized CuO sample:

(a) Cu 2p and (b) O 1s.

4.2.6 V-I Characteristic Curves

The electrical characteristic of the 15 min processed CuO deposited as film on alumina substrate has been investigated. The current values of the film were measured by applying voltage interval –20 V to 20 V at various temperatures. The results in the temperature range 200–300 ^{o}C operating in air is shown in Figure 4.21. The prepared films exhibited straight line characterization that relies on the major mechanism of ohmic current. In the ohmic region, the number of free carriers is higher than the number of applied charge carriers. Thus, free carriers have more influence in electrical conduction than the electrons which applied to semiconductors. The carrier diffusion in materials both forward and reverse bias is at the same mechanism. Specific contact resistivity (ρ_c) at the temperature of 200, 225, 250, 275 and 300 ^{o}C was calculated by the relationship of $\rho_c=V/j$ (j is the current density) which shows the results of $0.142x10^5$, $0.057\ x10^5$, $0.037\ x10^5$, $0.020\ x10^5$ and $0.014\ x10^5\ \Omega cm^2$, respectively. The specific contact resistivity was decreased when the temperature was increased because the thermal activation generated more free charge carriers.

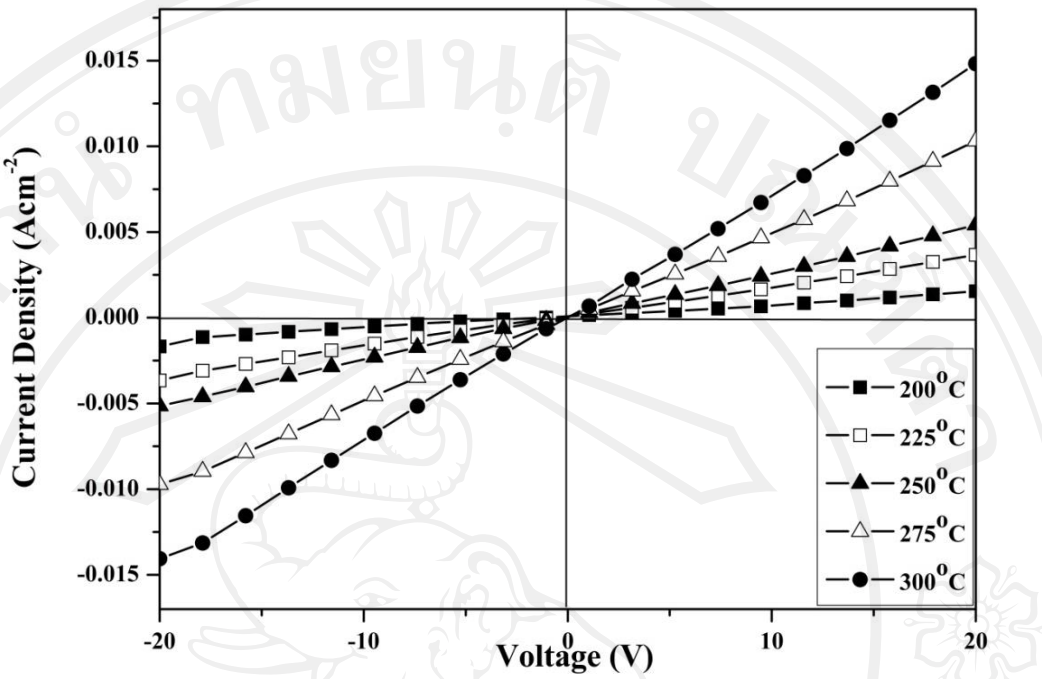

Figure 4.21 Symmetric current and voltage behavior for 15 min processed CuO at various temperatures.

4.2.7 Gas Sensing Measurement

The CuO sample processed for 15 min was exposed in ammonia-air locked chamber with 1,055 ppm concentration of NH_3 gas. The response of the sensor was studied by selecting the operating temperature in the range of 200–300ºC. For the results of Figure 4.22 and 4.23, sensitivity gradually increased when the temperature increased: at 200 ºC, 225 ºC and 250 ºC with the value of 18.5 %, 21.0 % and 21.9 % (highest), respectively. At 250 ºC operating temperature, the activation energy could be high enough to form a complete chemical reaction. Further increase of the temperature, more working temperature led to sensitivity decrease with the value of 16.3% at 275 ºC and 12.5% at 300 ºC because of desorption of oxygen ions at the surface. At the initial step while sensor exposing to the tested gas, the sensitivity abruptly increased to the highest value. Then, it went down to reach a new equilibrium point and held at this state.

The similar gas sensing behavior was reported by other researchers who studied nanostructured materials to NH_3 gas detection such as copper oxide nanowires [107], tungsten oxide nanowire films [108] and silver nanowires [109]. However, the first increase is unclear. The result could be the cause of distribution of the tested gas with heterogeneous spreading in the closed chamber that made more gas density at some parts and less gas density at others. Static gas testing system spends a time for gas homogeneous distribution.

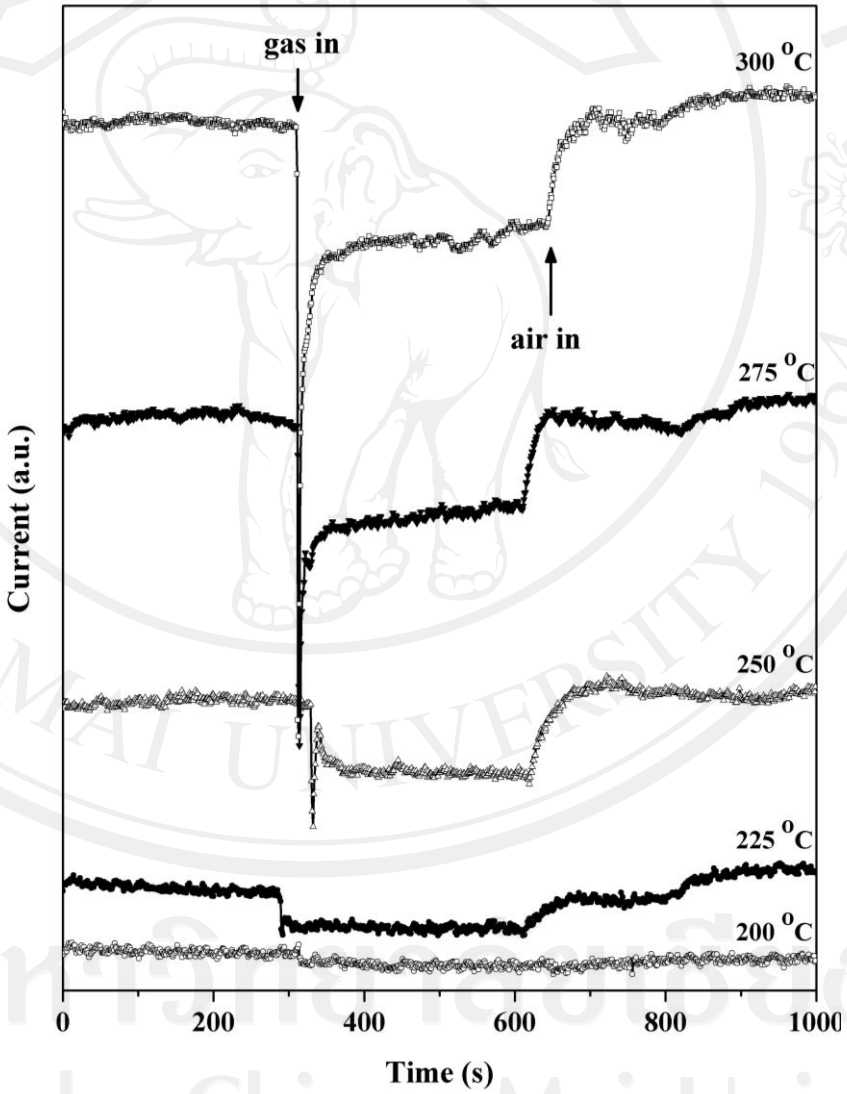

Figure 4.22 Dynamic respond-recovery curves of 15 min synthesized CuO at different working temperatures.

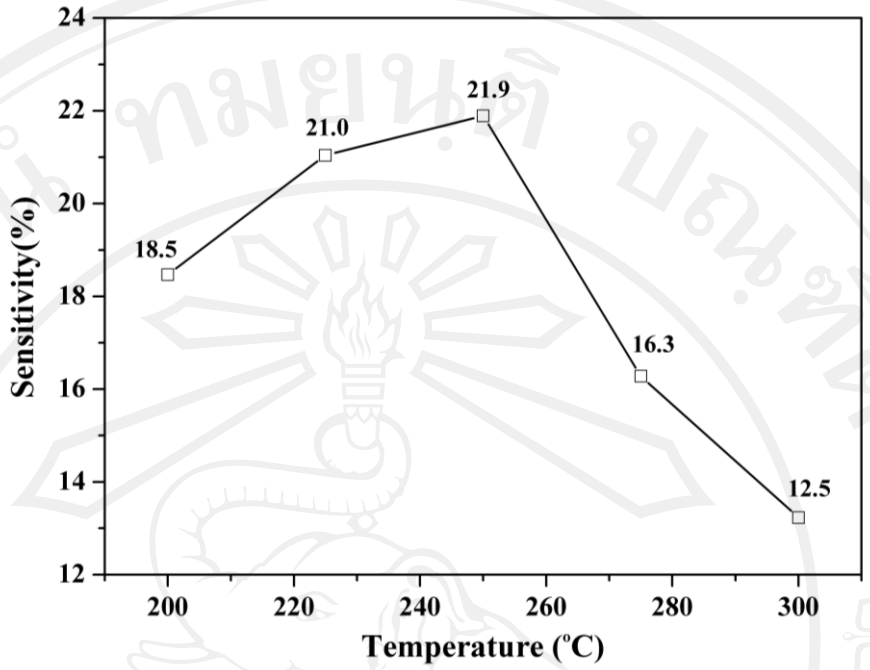

Figure 4.23 Sensitivity of 15 min processed CuO at various working temperatures.

The current density change of CuO gas sensor to NH_3 in air at various concentrations at 250 °C is shown in Figure 4.24. The sensitivity of gas sensor as a function of NH_3 concentration is shown in Figure 4.25. The linear increase of gas response with concentration increasing was clearly detected. Sensitivity values were found to be 21.9%, 30.2%, 32.1%, 51.0% and 56.6% by exposing to the NH_3-air gas mixture at concentration of 1055, 2110, 3165, 4220 and 5275 ppm of ammonia, respectively. These values were fitted to a linear regression line: S = 0.00856C + 11.28228, with C = ammonia concentration. At C = 10,000 ppm, the sensitivity (S) was calculated to be 96.88 %. The present sensitivity is very close to the report of Mashock [107]: gas sensing properties of CuO nanowires exposing to 10,000 ppm NH_3 gas concentration at room temperature without surface functionalization have a sensitivity of 92 % (evaluated from

the $\frac{R_{gas} - R_{air}}{R_{air}}$ x 100). The surface of the device can be improved by doping with nanoparticle catalyst.

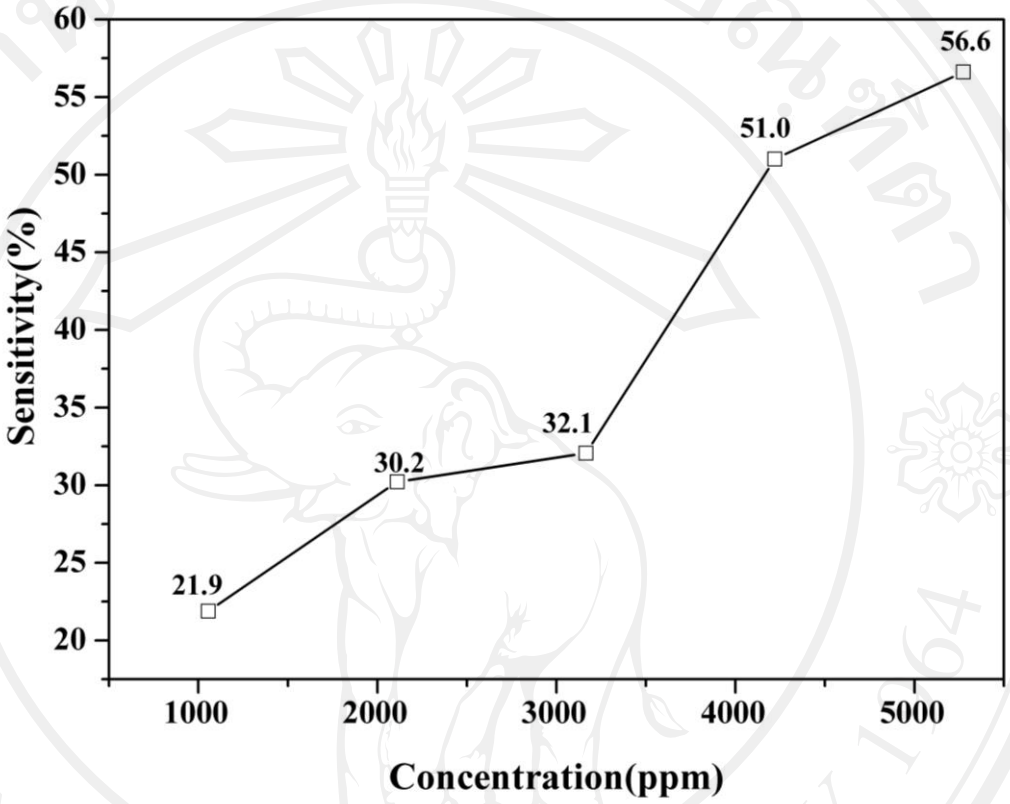

Figure 4.24 Current density characteristic of the 15 min as-synthesized CuO sample at different NH_3 concentrations.

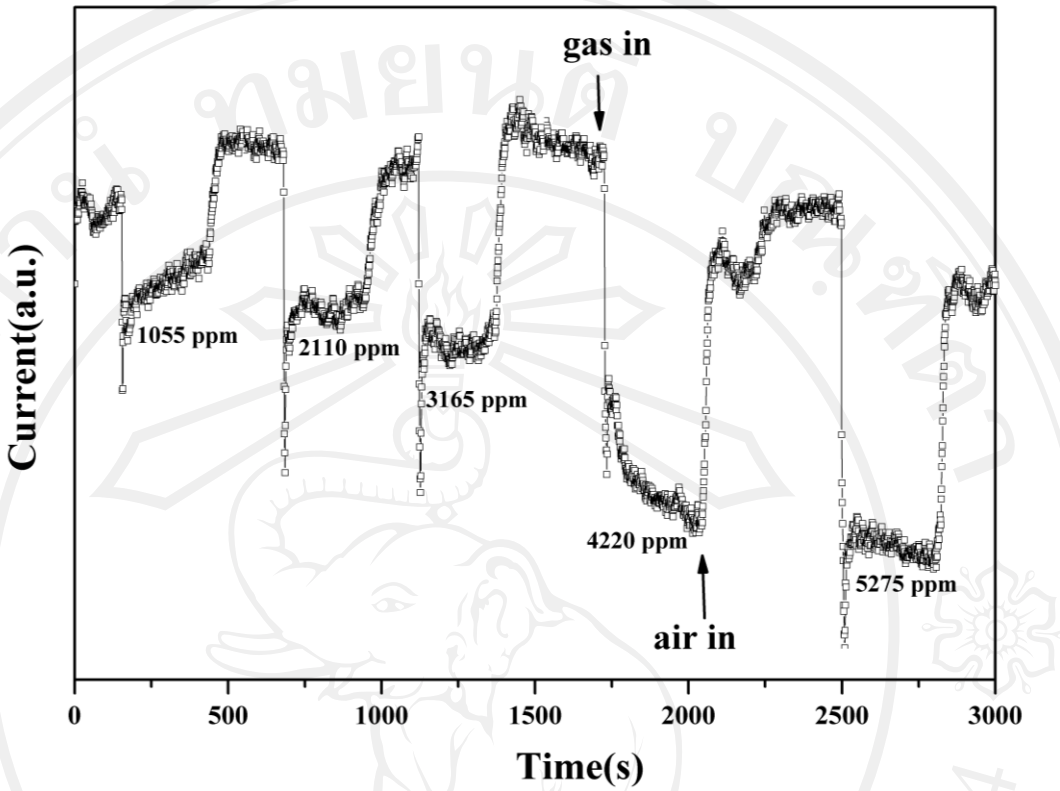

Figure 4.25 Sensitivity of the 15 min as-synthesized CuO sample at different NH_3 concentrations.

For the performance of metal oxide gas sensor to the tested gas, the main cause to electrical resistance change is adsorption and desorption of the detected gas at its surface [110]. Oxygen molecules adsorb on CuO at a temperature about 10^{o}C.These molecules were placed at surface defect sites as electron acceptors. The oxygen ionic species (O_2^-, O^- and O^{2-}) originally control by the working temperature, described by the following equations [111].

$$O_2(gas) \leftrightarrow O_2(ads) \quad (4.4)$$

$$O_2(ads) + e^- \leftrightarrow O_2^-(ads) \quad (4.5)$$

$$O_2^-(ads) + e^- \leftrightarrow 2O^-(ads) \quad (4.6)$$

CuO surface was attached by negative charge oxygen ions by the adsorbed and drawn electrons. Thus, holes near the surface increase and influence the increasing conduction as well. When NH_3 gas contaminated on surface, O^- reacted with the tested gas explained by the following equation [112].

$$2NH_3 + 3O^- \rightarrow 3H_2O + N_2 + 3e^- \quad (4.7)$$

The released electrons went back to valence band. Decreasing the concentration of holes generated the increase of resistance. When the tested gas was replaced by air, the sensor restored to original state.